Supporting Information

Controllable Synthesis of MOFs-derived Porous and Tubular Bimetallic Fe-Ni Phosphides for Efficient Electrocatalytic Water Splitting

Shumin Li,[†] Jingyun Wang,[†] Xiaoyu Lv, Song Zheng, Jin Wang and Zhengquan Li[*]

Key Laboratory of the Ministry of Education for Advanced Catalysis Materials, Zhejiang Normal University, Jinhua, Zhejiang 321004, P. R. China

[†] Equal contribution

*E-mail: zqli@zjnu.edu.cn (Z. Li)

1. Experimental

1.1 Synthesis of Fe$_x$Ni$_y$-MIL-88

All the reagents were in analytic grade and were purchased from Aladdin Industry Inc. (Shanghai, China) without further purification. The synthetic protocol of Fe$_x$Ni$_y$-MIL-88 nanorods was according to a previous report with slight modification.[1] Here we take the synthesis of Fe/Ni-MIL-88 with a Fe/Ni molar of 1:2 (denoted as FeNi$_2$-MIL-88) as an example. In a typical process, 0.333 mmol FeCl$_3$·6H$_2$O, and 1 mmol terephthalic acid were dissolved in 30 mL N,N-dimethylamphetamine (DMA). Then, 0.666 mmol Ni(NO$_3$)$_2$·6H$_2$O was added and stirred for 1 h. The solution was transferred into a 50-mL autoclave, sealed and heated to 150 °C. After maintaining at 150 °C for 3 h, the autoclave was naturally cooled down to room-temperature. Next, the precipitate was collected by centrifugation at a speed of 4000 rpm. After washed with DMA and ethanol twice, respectively, the product was collected and then dried at 80 °C in a vacuum overnight for further use.

Fe$_2$Ni-MIL-88 and FeNi-MIL-88, were prepared with a similar procedure to that of FeNi$_2$-MIL-88 described above, except that the molar ratios of FeCl$_3$·6H$_2$O to Ni(NO$_3$)$_2$·6H$_2$O are 2:1 and 1:1, respectively. We also prepared monometallic Fe-MIL-88 and Ni-MOF, using pure FeCl$_3$·6H$_2$O or Ni(NO$_3$)$_2$·6H$_2$O as the metal sources, respectively.

1.2 Synthesis of Fe$_x$Ni$_y$P porous nanoparticles

Fe$_x$Ni$_y$P porous nanoparticles (NPs) were synthesized by low-temperature phosphating process. When preparing the Fe$_x$Ni$_y$P NPs with Fe/Ni molar ratio of 1:2 (denoted as FeNi$_2$P-NPs), 20 mg as-prepared FeNi$_2$-MIL-88 were put into one side of a ceramic boat, and 1 g NaH$_2$PO$_2$·H$_2$O were put into the opposite side of the ceramic boat. The distance between these two samples was about 2 cm to avoid being mixed. The ceramic boat was placed in a tube furnace under N$_2$ atmosphere. The boat was then heated to 350 °C with a ramp rate of 2 °C·min^{-1} and kept at this temperature for 3 h. After the furnace was cooled to room temperature, the FeNi$_2$P-NPs product was obtained.

Fe$_2$P-NPs, Fe$_2$NiP-NPs, FeNiP-NPs, FeNi$_3$P-NPs and Ni$_2$P-NPs were also synthesized by a similar procedure to that of FeNi$_2$P-NPs described above, except that Fe-MIL-88, Fe$_2$Ni-MIL-88, FeNi-MIL-88, FeNi$_3$-MIL-88 and Ni-MOF were used as the precursors, respectively.

1.3 Synthesis of Fe$_x$Ni$_y$P nanotubes

The synthesis of Fe$_x$Ni$_y$P nanotubes (NTs) is similar to that of Fe$_x$Ni$_y$P-NPs except that the temperature for the phosphating process is 300 °C. Fe$_2$P-NTs, Fe$_2$NiP-NTs, FeNiP-NTs, FeNi$_2$P-NTs, FeNi$_3$P-NTs and Ni$_2$P-NTs were synthesized with Fe-MIL-88, Fe$_2$Ni-MIL-88, FeNi-MIL-88, FeNi$_2$-MIL-88, FeNi$_3$-MIL-88 and Ni-MOF were used as the precursors, respectively.

1.4 Characterizations

Field-emission scanning electron microscopy (FESEM) was performed on a Hitachi S-4800 SEM. Transmission electron microscopy (TEM) and element mappings were conducted on a JEOL 2010F TEM. Powder X-ray diffraction (XRD) was carried out on a Philips X' Pert Pro X-ray diffractometer equipped with a Cu Kα radiation. X-ray photoelectron spectroscopy (XPS) was performed on an ESCALab MKII X-ray photoelectron spectrometer equipped with Mg-Kα X-ray radiation. Brunauer-Emmett-Teller (BET) surface areas of samples were measured on a micrometritics ASAP 2020 physisorption analyzer at 77 K.

1.5 Electrochemical measurements

The electrochemical measurements were performed on a CHI760E electrochemical workstation (CH instrument, China) with a three-electrode configuration. A glassy carbon electrode (GCE, 5 mm in diameter) was used as the support for the working electrode. Hg/HgO electrode and graphite rod acted as the reference electrode and counter electrode, respectively. For the fabrication of working electrodes, 5 mg of the catalysts were dispersed in 1 mL mixed solution containing 500 μL ethanol, 460 μL deionized water and 40 μL Nafion solution (5 wt%). Then, the mixture was ultrasonically treated for 30 min till forming a homogeneous catalyst ink. Afterwards, 10 μL of the catalyst inks was dropped on the polished GC electrode and dried at room temperature.

The OER performance was evaluated in O$_2$-saturated 1 M KOH solution, while the HER performance was evaluated in the N$_2$-saturated 1 M KOH solution. Linear sweep voltammetry (LSV) was recorded at a scan rate of 5 mV s^{-1}. Electrochemical double-layer capacitances (C$_{dl}$) were determined by cyclic voltammetry (CV) method through varying the scan rate (10, 20, 40, 60, 80 and 100 mV s^{-1}) in the non-Faradaic region from -0.05 to 0.05 V *vs*. Hg/HgO. Electrochemical impedance spectroscopy (EIS) was measured from 10^5 to 0.1 Hz with an amplitude of 5 mV. The overall water splitting performance was evaluated in 1 M KOH using a two-electrode configuration.

All the measured potentials in this work were performed with iR compensation and converted to reverse hydrogen electrode (RHE): $E_{RHE} = E_{Hg/HgO} + 0.059\ pH + 0.098$.
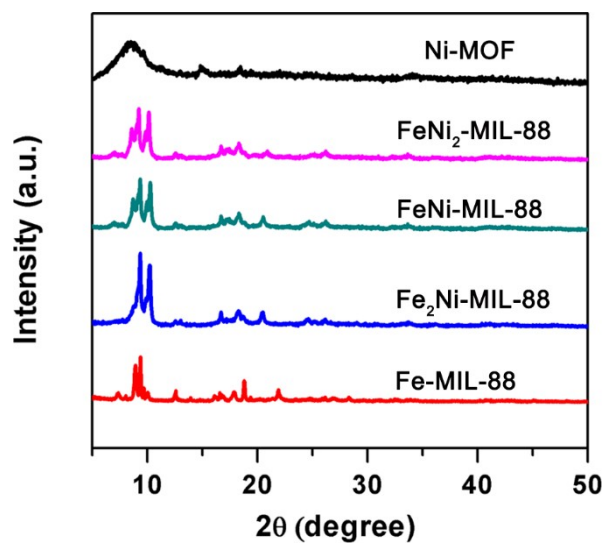
Figure S1. XRD patterns of Fe_xNi_y-MIL-88.

Bi-Fe/Ni MOFs have the similar crystal structure as Fe-MIL-88, indicating the bi-MOFs were successfully prepared.   While Ni-MOF is in different structure from Fe-MIL-88 and other bi-MOFs.
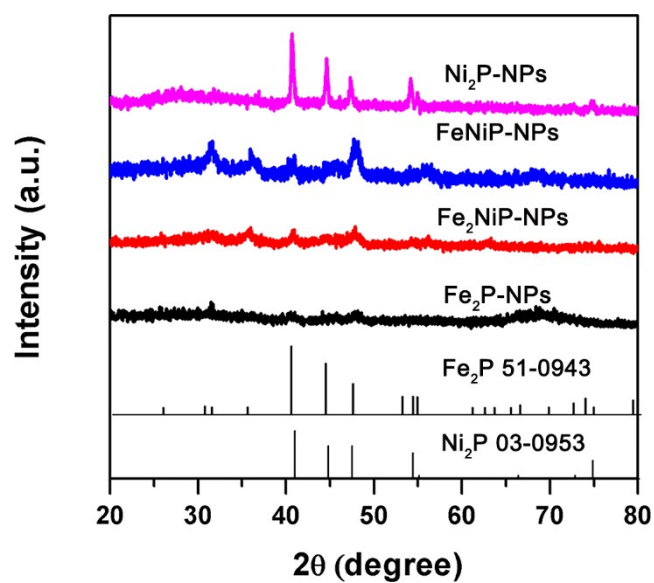
Figure S2. XRD patterns of Fe_xNi_yP-NPs.

It can be seen that Fe_2P and Ni_2P have the nearly similar crystal structure. There are only one set of XRD pattern of both FeNiP and Fe_2NiP, respectively. The XRD patterns of FeNiP and Fe_2NiP are between the peaks of Fe_2P and Ni_2P, indicating the formation of alloy phase.
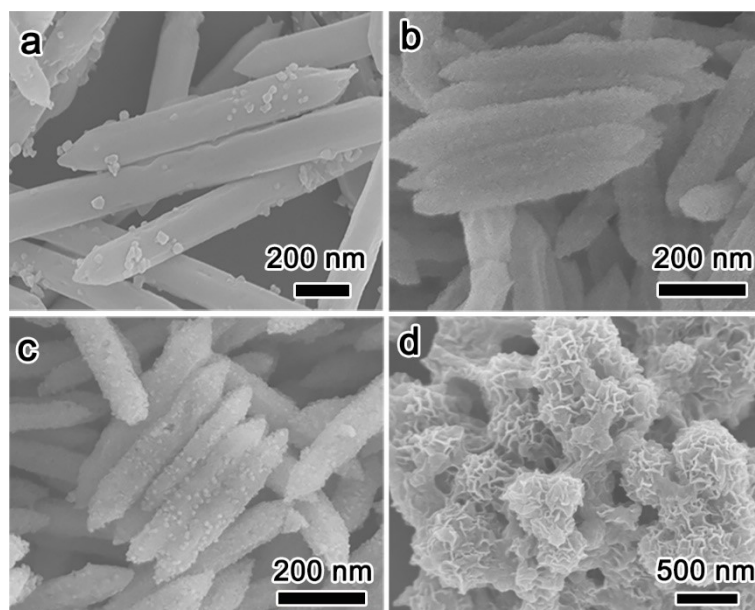
Figure S3. SEM images of samples: (a) Fe_2P-NPs, (b) Fe_2NiP- NPs, (c) FeNiP-NPs and (d) Ni_2P-NPs.
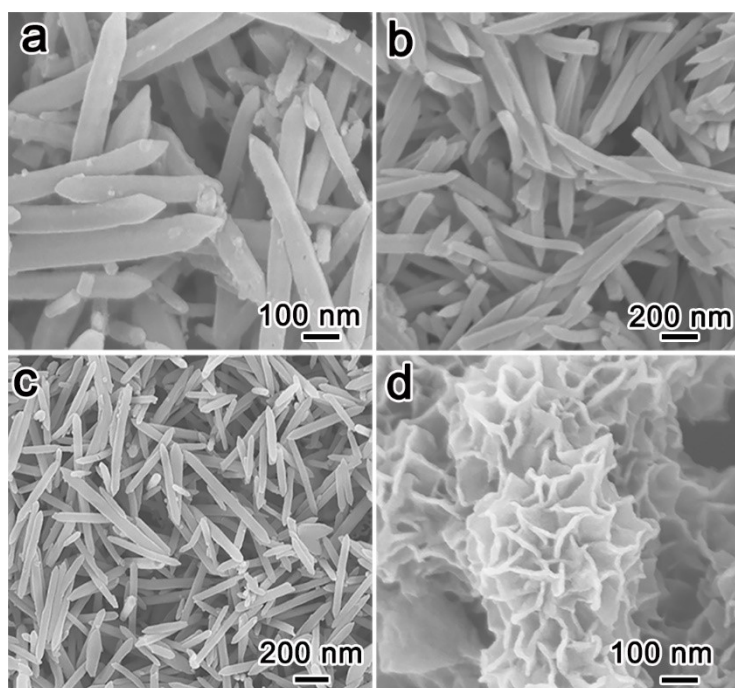
Figure S4. SEM images of (a) Fe-MIL-88, (b) Fe$_2$Ni-MIL-88, (c) FeNi-MIL-88 and (d) Ni-MOF.

It can be seen that Fe-MIL-88 and the bi-Fe/Ni MOFs show a uniform nanorod morphology and the similar sizes, while Ni-MOF shows a nanoflower morphology.
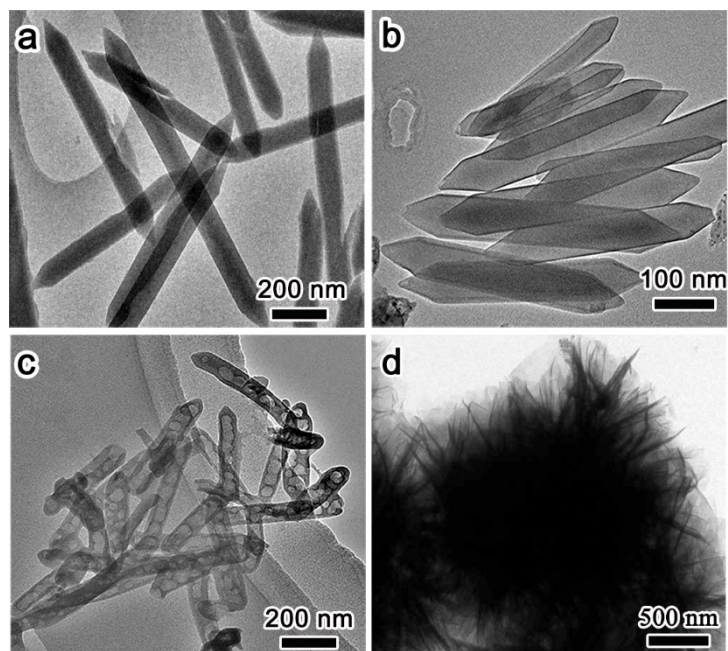
Figure S5. TEM images of samples: (a) Fe_2P-NTs, (b) Fe_2NiP-NTs, (c) FeNiP-NTs, (d)Ni_2P-NTs.
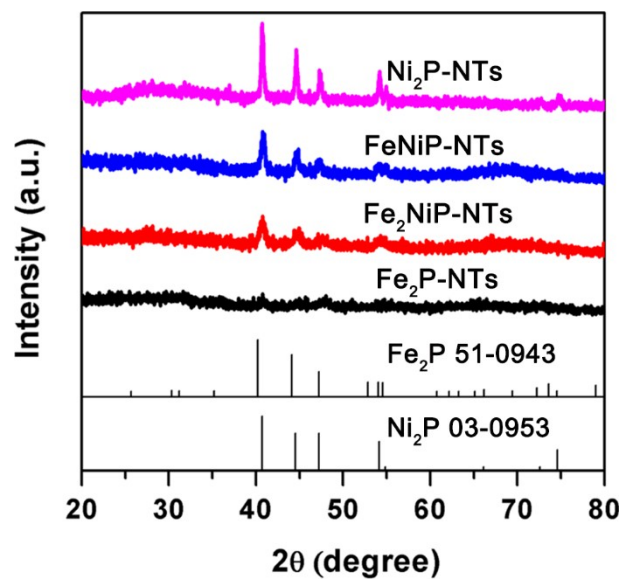
Figure S6. XRD patterns of Fe_xNi_yP-NTs.

Though the morphologies are different from Fe_xNi_yP-NPs, the crystal structures of Fe_xNi_yP-NTs are nearly identical as the Fe_xNi_yP-NPs counterparts.
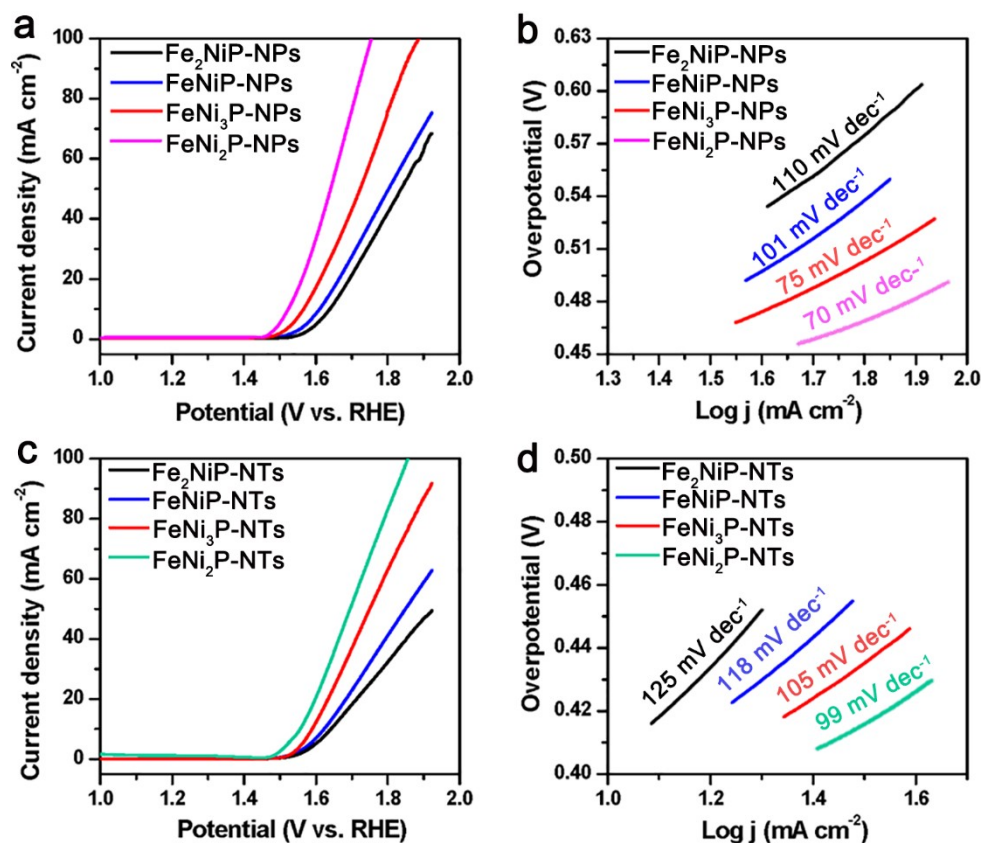
Figure S7. OER performances: (a) LSV curves and (b) Tafel plots of Fe_xNi_yP-NPs; (c) LSV curves and (d) Tafel plots of Fe_xNi_yP-NTs.

When adjusting the Fe/Ni ratio, the OER activity can be tuned further.   Increasing the Ni ratio in bimetallic phosphides, the OER performance gets elevated firstly, but then declined.   Among the samples with different metal ratios, $FeNi_2P$ exhibits the best OER activity in both morphologies.   The same trend of electrocatalytic activity in both morphologies indicates that the electronic structure of $FeNi_2P$ is more appropriate for OER.
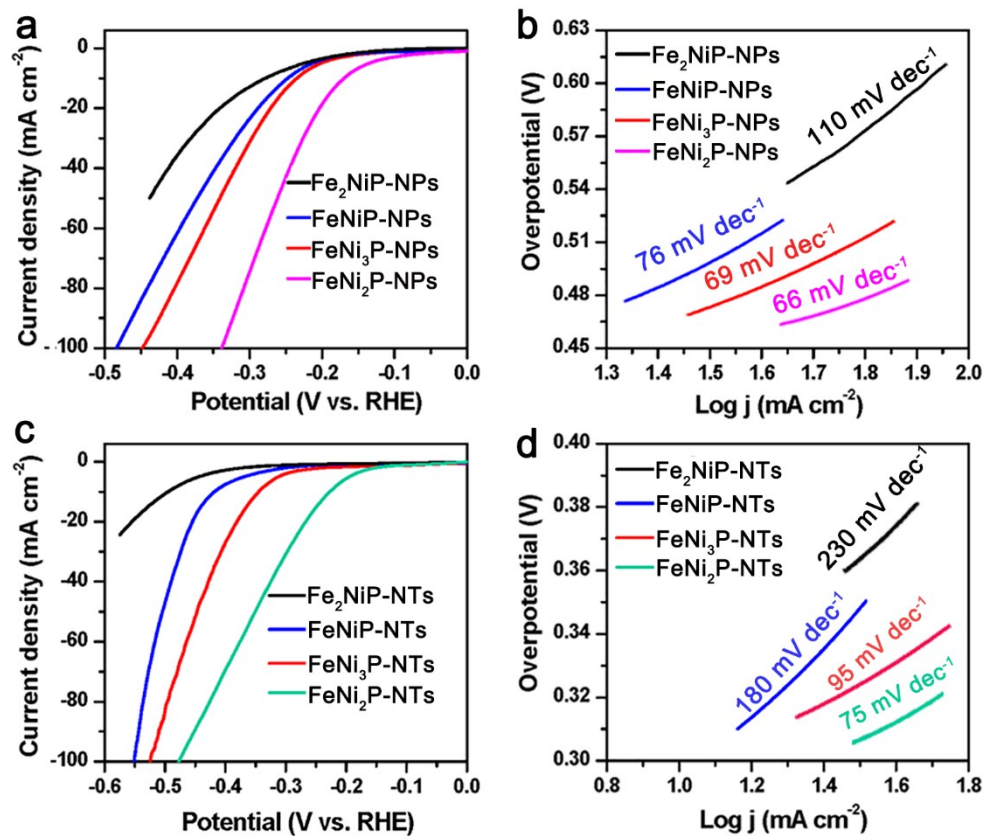
Figure S8. HER performances: (a) LSV curves and (b) Tafel plots of Fe_xNi_yP-NPs; (c) LSV curves and (d) Tafel plots of Fe_xNi_yP-NTs.

The HER activity can be further tuned by regulating the Fe/Ni ratio in Fe_xNi_yP samples, indicating it is an effective strategy to prepare composite electrocatalysts for HER. The trend of HER performance is similar as OER, and $FeNi_2P$ in both morphologies exhibit the best HER activity among these samples. Considering the too strong hydrogen absorption ability of pristine Fe_2P and the too weak hydrogen absorption of pristine Ni_2P,[2] the hydrogen absorption ability of the sample would get more appropriate for HER when combine these two components for the composites.
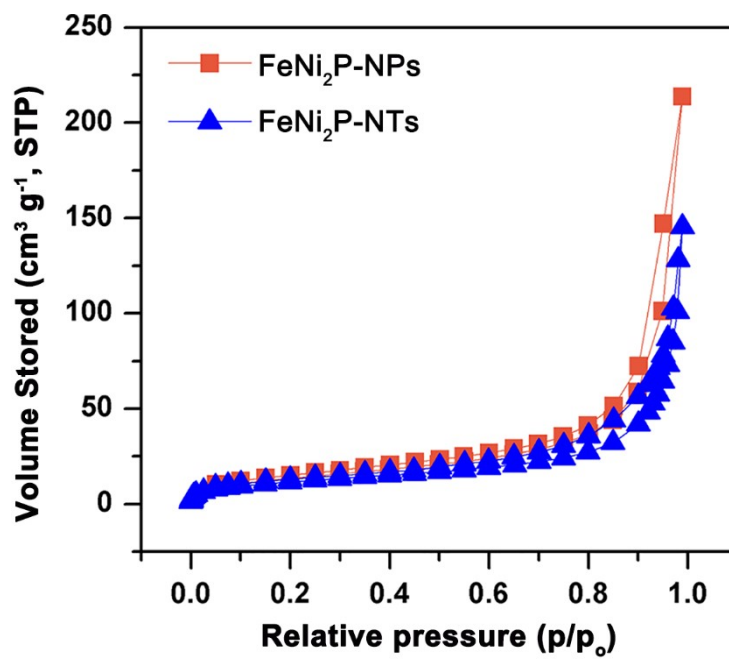
Figure S9. BET surface area of FeNi$_2$P-NPs and FeNi$_2$P-NTs.
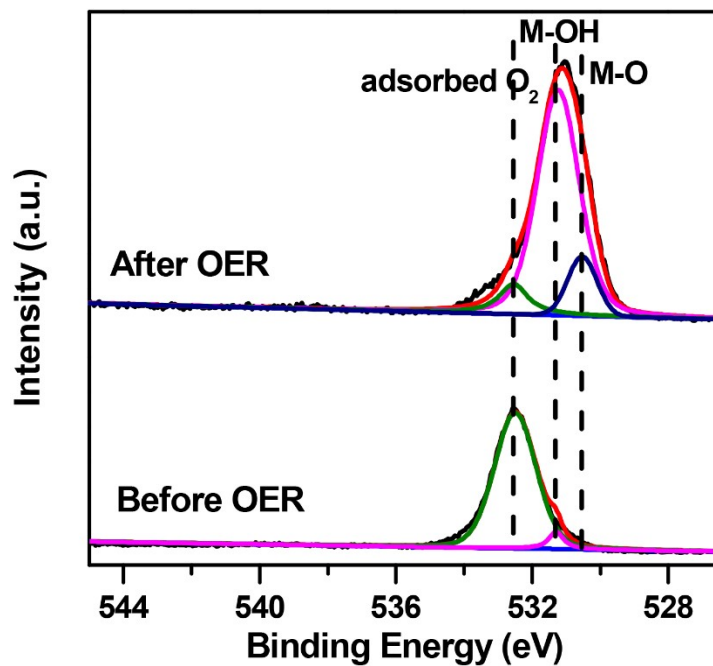
Figure S10. High-resolution XPS spectra in the range of O1s for FeNi$_2$P-NPs.

According to previous reports, after OER, some species of metal oxides and metal hydroxides can be observed on the surface of TMPs in several cases, implying that the OER process matches a proton-coupled electron transfer route.[3-7]

Table S1. Comparison of OER performance for TMPs in 1 M KOH.

TMPs	Tafel slope (mV dec^{-1})	$\eta_{j = 10\ mA\ cm^{-2}}$ (mV)	Ref.
FeNi$_2$P-NPs	70	286	this work
Carbon fiber @ NiP$_x$	54.7	200	8
CoP nanosheet/carbon	85.6	277	9
Ni-P nanoparticles/Ni foam	58	309	10
Co–P nanospheres/FTO	83	420	11
CoP nanoneedles/carbon cloth	62	281	12
CoP$_3$ nanoneedle arrays/carbon fiber paper (CFP)	62	344	13

Table S2. Comparison of HER performance for TMPs in 1M KOH.

TMPs	Tafel slope (mV dec^{-1})	$\eta_{j = 10\ \text{mA cm}^{-2}}$ (mV)	Ref.
FeNi$_2$P-NPs	66	170	this work
Ni$_3$P porous hollow nanospheres (PHNs)	190	$\eta_{20} = 338$	14
Ni$_2$P nanoparticles	100	$\eta_{20} = 250$	15
NiP$_2$ nanosheet/carbon cloth	65	102	16
MoP-hemispheres/carbon cloth	64	121	17
MoP$_2$ nanoparticles/Mo	80	194	18
FeP nanowires	75	194	19
FeP nanowires/carbon fiber paper	134	181	20

References

1   S. Li, J. Tan, Z. Jiang, J. Wang, Z. Li, MOF-derived bimetallic Fe-Ni-P nanotubes with tunable compositions for dye-sensitized photocatalytic H_2 and O_2 production, *Chem. Eng. J.*, 2020, **384**, 123354.

2   Y. Wang, B. Kong, D. Zhao, H. Wang, C. Selomulya, Strategies for developing transition metal phosphides as heterogeneous electrocatalysts for water splitting, *Nano Today*, 2017, **15**, 26-55.

3   T.R. Cook, D.K. Dogutan, S.Y. Reece, Y. Surendranath, T.S. Teets, D.G. Nocera, Solar energy supply and storage for the legacy and nonlegacy worlds, *Chem Rev.*, 2010 **110**, 6474-502.

4   A. Grimaud, O. Diaz-Morales, B. Han, W.T. Hong, Y. Lee, L. Giordano, K.A. Stoerzinger, M.T.M. Koper, S. Yang, Activating lattice oxygen redox reactions in metal oxides to catalyse oxygen evolution, *Nat. Chem.,* 2017, **9**, 457–465.

5   N.T. Suen, S.F. Hung, Q. Quan, N. Zhang, Y.J. Xu, H.M. Chen, Electrocatalysis for the oxygen evolution reaction: recent development and future perspectives. *Chem. Soc. Rev.*, 2017, **46**, 337–365.

6   S. Zhao, R. Jin, H. Abroshan, C. Zeng, H. Zhang, S.D. House, E. Gottlieb, H.J. Kim, J.C. Yang, R. Jin, Gold Nanoclusters Promote Electrocatalytic Water Oxidation at the Nanocluster/$CoSe_2$ Interface, *J. Am. Chem. Soc.*, 2017, **139**, 1077–1080.

7   T. Reier, H.N. Nong, D. Teschner, R. Schlögl, P. Strasser, *Adv. Energy Mater.*, 2017, **7**, 1601275.

8   Z. Zhang, S. Liu, J. Xiao, S. Wang, Fiber-based multifunctional nickel phosphide electrodes for flexible energy conversion and storage, *J. Mater. Chem. A*, 2016, **4**, 9691-9699.

9   J. Chang, L. Liang, C. Li, M. Wang, J. Ge, C. Liu, W. Xing, Ultrathin cobalt phosphide nanosheets as efficient bifunctional catalysts for a water electrolysis cell and the origin for cell performance degradation, *Green Chem.*, 2016, **18**, 2287-2295.

10 C. Tang, A.M. Asiri, Y. Luo, X. Sun, Electrodeposited Ni-P alloy nanoparticle films for efficiently catalyzing hydrogen- and oxygen-evolution reactions, *ChemNanoMat* 2015, **1**, 558.

11   G.-Q. Han, X. Li, Y.-R. Liu, B. Dong, W.-H. Hu, X. Shang, X. Zhao, Y.-M. Chai, Y.-Q. Liu, C.-G. Liu, Controllable synthesis of three dimensional electrodeposited Co–P nanosphere arrays as efficient electrocatalysts for overall water splitting, *RSC Adv.*, 2016, **6**, 52761-52771.

12   P. Wang, F. Song, R. Amal, Y.H. Ng, X. Hu, Efficient water splitting catalyzed by cobalt phosphide-based nanoneedle arrays supported on carbon cloth, *ChemSusChem* 2016, **9**, 472.

13   T. Wu, M. Pi, D. Zhang, S. Chen, 3D structured porous CoP_3 nanoneedle arrays as an efficient bifunctional electrocatalyst for the evolution reaction of hydrogen and oxygen, *J. Mater. Chem. A*, 2016, **4**, 14539-14544.

14   L. Jin, H. Xia, Z. Huang, C. Lv, J. Wang, M.G. Humphrey, C. Zhang, Phase separation synthesis of trinickel monophosphide porous hollow nanospheres for efficient hydrogen evolution, *J. Mater. Chem. A* 2016, **4**, 10925–10932.

15   L. Feng, H. Vrubel, M. Bensimon, X. Hu, Easily-prepared dinickel phosphide (Ni_2P) nanoparticles as an efficient and robust electrocatalyst for hydrogen evolution, *Phys. Chem. Chem. Phys.*, 2014, **16**, 5917-5921.

16   P. Jiang, Q. Liu, X. Sun, NiP_2 nanosheet arrays supported on carbon cloth: an efficient 3D hydrogen evolution cathode in both acidic and alkaline solutions, *Nanoscale*, 2014, **6**, 13440-13445.

17   C. Deng, J. Xie, Y. Xue, M. He, X. Wei, Y.-M. Yan, Synthesis of MoP decorated carbon cloth as a binder-free electrode for hydrogen evolution, *RSC Adv.*, 2016, **6**, 68568-68573.

18   Z. Pu, I. Saana Amiinu, M. Wang, Y. Yang, S. Mu, Semimetallic MoP_2: an active and stable hydrogen evolution electrocatalyst over the whole pH range, *Nanoscale*, 2016, **8**, 8500-8504.

19   C.Y. Son, I.H. Kwak, Y.R. Lim, J. Park, FeP and FeP_2 nanowires for efficient electrocatalytic hydrogen evolution reaction, *Chem. Commun.*, 2016, **52**, 2819-2822.

20   C. Lv, Z. Peng, Y. Zhao, Z. Huang, C. Zhang, The hierarchical nanowires array of iron phosphide integrated on a carbon fiber paper as an effective electrocatalyst for hydrogen generation, *J. Mater. Chem. A*, 2016, **4**, 1454-1460.